Electrocatalysis (2018) 9:333–342
https://doi.org/10.1007/s12678-017-0435-1

ORIGINAL RESEARCH

Electrochemical Investigation of the Hydrogen Evolution Reaction on Electrodeposited Films of $Cr(OH)_3$ and Cr_2O_3 in Mild Alkaline Solutions

Adriano S. O. Gomes[1,2] · **Nina Simic**[2] · **Mats Wildlock**[2] · **Anna Martinelli**[3] · **Elisabet Ahlberg**[1]

Published online: 6 November 2017

Abstract The hydrogen evolution reaction (HER) from water reduction is the main cathodic reaction in the sodium chlorate process. The reaction typically takes place on electrodes covered with a Cr(III) oxide-like film formed in situ by reduction of sodium dichromate in order to avoid reduction of hypochlorite and thereby increase the selectivity for the HER. However, the chemical structure of the Cr(III) oxide-like film is still under debate. In the present work, the kinetics of the HER were studied using titanium electrodes covered with electrodeposited $Cr(OH)_3$ or Cr_2O_3, which were characterized by means of scanning electron microscopy (SEM), energy-dispersive x-ray spectroscopy (EDX), x-ray photoelectron spectroscopy (XPS), and Raman spectroscopy. A clear difference in the morphology of the deposited surfaces was obtained, and the structure could be revealed with Raman spectroscopy. The kinetics for the HER were investigated using potentiodynamic and potentiostatic techniques. The results show that the first electron transfer is rate limiting and that the activity decreases in the order Cr_2O_3@Ti > bare Ti > $Cr(OH)_3$@Ti. The low activity obtained for $Cr(OH)_3$@Ti is discussed in terms of the involvement of structural water in the HER and the slow ligand exchange rate for water in Cr(III) complexes, while the high activity obtained for Cr_2O_3@Ti is rationalized by a surface area effect in combination with reduction of surface water and water in solution.

Keywords Electrocatalysis · Raman spectroscopy · Sodium chlorate · Electrodeposition

Electronic supplementary material The online version of this article (https://doi.org/10.1007/s12678-017-0435-1) contains supplementary material, which is available to authorized users.

✉ Elisabet Ahlberg
ela@chem.gu.se

[1] Department of Chemistry and Molecular Biology, University of Gothenburg, Kemigården 4, SE-412 96 Gothenburg, Sweden

[2] AkzoNobel Pulp and Performance Chemicals, SE-445 80 Bohus, Sweden

[3] Department of Chemistry and Chemical Engineering, Chalmers University of Technology, Kemigården 4, SE-412 96 Gothenburg, Sweden

Introduction

The electrosynthesis of sodium chlorate is one of the most important industrial processes, especially for the pulp and paper industry [1]. The production of chlorate occurs via the electrolysis of sodium chloride and water (Eq. 1). Electricity is the main driving force of electrolysis and accounts for up to 70% of the total production cost [2]. The main by-products are heat and hydrogen gas, which can be re-used in the process or surroundings [2]. Chlorate is further reduced to form chlorine dioxide (Eq. 2), the state-of-the-art bleaching chemical for kraft pulp [1, 3].

$$NaCl + 3H_2O \xrightarrow{6e^-} NaClO_3 + 3H_2 \quad (1)$$

$$2NaClO_3 + H_2O_2 + H_2SO_4 \rightarrow 2ClO_2 + O_2 + Na_2SO_4 + 2H_2O \quad (2)$$

The electrochemical and chemical reactions yielding chlorate have been well described in the literature [4–11]. The main half reactions are the cathodic reduction of water (Eq. 3) and the anodic chloride oxidation (Eq. 4). The formation of chlorate occurs in the bulk of the electrolyte as follows: Cl_2 immediately undergoes hydrolysis

forming hypochlorous acid and chloride (Eq. 5); hypochlorous acid is in equilibrium with hypochlorite (Eq. 6) while chlorate is produced from a disproportionation reaction between hypochlorous acid and hypochlorite (Eq. 7). The optimum pH for the process is empirically known to be between 6 and 7 [12]. At this pH, the equilibrium in Eq. 6 is shifted to the left, keeping the chlorate formation (Eq. 7) at its highest rate.

$$2H_2O + 2e^- \rightarrow H_2 + 2OH^- \quad E° = -0.828 \text{ V vs.NHE} \tag{3}$$

$$2Cl^- \rightarrow Cl_2 + 2e^- \quad E° = +1.360 \text{ V vs.NHE} \tag{4}$$

$$Cl_2 + H_2O \leftrightarrow HClO + H^+ + Cl^- \quad (bulk) \tag{5}$$

$$HClO \leftrightarrow H^+ + ClO^- \quad (bulk, \text{pKa} = 7.5) \tag{6}$$

$$2HClO + ClO^- \rightarrow ClO_3^- + Cl^- + 2H^+ \quad (bulk) \tag{7}$$

Chlorate is produced in undivided cells, using mild steel cathodes and dimensionally stable anodes (DSA) [2]. The electrolyte is rich in ions such as chloride, chlorate, and hypochlorite ($HClO + ClO^-$) [2]. In this setup, water reduction competes with the cathodic reductions of chlorate and hypochlorite (Eqs. 8 and 9), which are thermodynamically favorable. Therefore, in chlorate electrolytes, the addition of sodium dichromate is necessary as it provides selectivity towards water reduction (note that the mild steel electrodes are not selective). Dichromate is cathodically reduced forming a chromium(III) oxide-like film, which inhibits the reactions given in Eqs. 8 and 9 [13, 14]. The composition and effects of such a film concerning chlorate electrochemistry has been investigated [4, 8, 15–17]. Other works, not directly related to the chlorate process, can be found in [18–20].

$$ClO^- + H_2O + 2e^- \rightarrow Cl^- + 2OH^- \quad E° = +0.89 \text{ V vs NHE} \tag{8}$$

$$ClO_3^- + 3H_2O + 6e^- \rightarrow Cl^- + 6OH^- \quad E° + 1.45 \text{ V vs NHE} \tag{9}$$

The use of sodium dichromate, even though optimum from the process point of view, is undesirable owing to the presence of Cr in the hexavalent form (Cr(VI)), which is poisonous, carcinogenic, reprotoxic, and mutagenic. Comprehensive reviews on the toxicity of Cr(VI) can be found in [21, 22]. The removal of chromium(VI) from chlorate electrolytes has long been pursued, and is even more motivated now, since Cr(VI) compounds were included in the REACH list Annex XIV to be banned for use in industrial processes in Europe [23], unless a special authorization is given.

Replacing sodium dichromate, however, is not an easy and straightforward task, and considerable efforts have been spent to find a suitable and more environmental friendly chemical to replace Cr(VI). Rare earth metal salts presented promising results in bench-scale experiments [24–26], but their solubility in a chlorate electrolyte [24] and/or low efficiency in long-term experiments [26] limit their application in real processes. Another option is the use of molybdate in the electrolyte. Molybdate is also reduced in situ and favors water reduction over chlorate and hypochlorite reduction. But molybdate ions interfere with the anodic reactions increasing the O_2 concentration in the cell gas [27], thus creating a safety issue. As an alternative to soluble molybdate, MoO_2 nanoparticles have been immobilized onto Ti and Fe electrodes in a Cr_2O_3 matrix, yielding a surface very selective towards water reduction in the presence of hypochlorite [28]. However, it was shown elsewhere that electrodeposited Cr_2O_3 completely prevents hypochlorite reduction on Ti electrodes [11] and, hence, the effects of MoO_2 particles as presented in [28] cannot be precisely evaluated.

It turns out that to find a suitable replacement for sodium dichromate, a deeper knowledge of the selective mechanism is necessary. In this context, a recent paper focusing on $Cr(OH)_3$ and Cr_2O_3 surfaces has shown that both are capable of blocking hypochlorite reduction, probably due to the p-type semi-conducting properties of Cr(III) oxide-like surfaces [11]. However, studies regarding water reduction on such films were not deeply investigated. With the aim to fill this gap, the present paper provides a comprehensive investigation of the mechanism and kinetics of water reduction on $Cr(OH)_3$- and Cr_2O_3-electrodeposited films. Notably, the idea of depositing Cr(III) oxide-like films offers the opportunity to characterize them prior to electrochemical analysis, and thus interpret the results based on the films' structure and composition.

Experimental

Electrode Preparation

Working rotating disk electrodes were home-made by molding Ti disks, with a 1-cm^2 geometrical surface area, in epoxy, referred in the text as Ti. The electrodes were used as the substrate for electrodeposition of $Cr(OH)_3$ and Cr_2O_3 films, henceforth referred to as $Cr(OH)_3$@Ti and Cr_2O_3@Ti, respectively.

Prior to electrodeposition, Ti substrates were polished with SiC paper (Struers) and later with alumina slurries (OP-AN Struers) until mirror-like surfaces were obtained. To remove any contamination from the polishing steps, the electrodes were ultrasonicated in Milli-Q water for at least 10 min. The Ti electrodes were etched in a HF solution (3.5 mM in H_2O, BASF) for 10 s, rinsed, and then directly immersed into the deposition solution.

$Cr(OH)_3$ and Cr_2O_3 were electrodeposited from two different Cr(VI) solutions as previously described by Aguilar et al. [29] (Table 1). The electrolyte for $Cr(OH)_3$ deposition consists of CrO_3 (Sigma-Aldrich) and $BaCO_3$ (Sigma-Aldrich). For Cr_2O_3 electrodeposition, the electrolyte consists of the same

Table 1 Composition of the electrolyte used for the deposition of Cr(III) oxide and hydroxide films [29]

	$Cr(OH)_3$	Cr_2O_3
CrO_3 (g/L)	364	364
$BaCO_3$ (g/L)	9.1	9.1
H_2SiF_6 (g/L)	–	1.8
KNO_3 (g/L)	–	2.3

CrO_3 and $BaCO_3$ with the addition of H_2SiF_6 (20–23.5 mM in H_2O; Sigma-Aldrich) and KNO_3 (Merck). The deposition potential was maintained at − 1.60 V (vs Ag/AgCl) during a period of 30 min using a PGSTAT12 Potentiostat (Autolab). The excess of solution was rinsed several times with Milli-Q water, and the electrodes were stored immersed in Milli-Q water.

Electrochemical Experiments

All electrochemical measurements were performed using a Gamry600™ potentiostat. The three-electrode glassy cell configuration was used, where a high-surface area platinum mesh was used as counter-electrode and the reference electrode was a double-junction Ag/AgCl (KCl 3 M, Metrohm, E = + 0.210 V vs nhe). Potential sweeps were recorded between 0.0 and − 2.2 V (vs Ag/AgCl) at 50 mV s^{-1} to investigate surface stability. Capacitive currents were measured between 0.0 and − 0.8 V (vs (Ag/AgCl) to estimate the capacitance of $Cr(OH)_3$- and Cr_2O_3-electrodeposited films.

Potentiostatic sweeps from − 0.2 to − 2.2 V (vs Ag/AgCl) in potential steps of − 0.1 V were also performed. At the same time, electrochemical impedance spectroscopy (EIS) measurements were carried out at every potential. EIS frequencies varied between 100 kHz and 10 mHz. For impedance experiments, the working electrode was placed in the centre of a round platinum mesh to improve the electrochemical response.

Cyclic voltammetry (CV), potentiostatic sweeps, and EIS were performed in de-aerated 0.2 M Na_2SO_4 at pH 11. The pH adjustment was made with addition of NaOH; N_2 gas flow was maintained in the top of the cell to prevent dissolution of O_2 in the electrolyte during experiments.

Surface Characterization

The surface morphology and composition were investigated with scanning electron microscopy (SEM) and energy-dispersive X-ray spectroscopy (EDX) in a LEO Ultra 55 FEG SEM equipped with Oxford Inca EDX system. The molecular structure of the films was analyzed with Raman spectroscopy using an InVia Reflex spectrometer from Renishaw. The excitation source was the 532-nm line of a diode laser, which together with a grating of 2400 lines per millimeter gives a spectral resolution better than 1 cm^{-1}. The presented Raman spectra are the result of 10 scans with a duration of 10 s each, if not otherwise stated. X-ray diffraction (XRD) was performed using a Siemens D5000 Diffractometer with a Bragg-Brentano setup equipped with a Cu k_α X-ray source and a scintillation detector from 20° to 63° at 0.100° intervals of 2θ, and cumulated count time of 4 s for each step.

Results and Discussion

Surface Characterization

In electrochemistry, the determination of surface composition and surface area is a prerequisite for a complete investigation of mechanisms and kinetic parameters. However, the investigation of Cr(III) films formed during the chlorate electrolysis was always limited by the uncertainty of the surface composition. For instance, for a long time it was believed that the reduction of chromate yields a hydrated $Cr(OH)_3$ film on platinum and gold [15] electrodes, but recently Hatch and Gewirth [20] determined with in situ Raman spectroscopy and atomic force microscopy (AFM) that the structure of chromate electrochemically reduced on gold is in fact a Cr_2O_3 thin film. In addition, a dual composition of the film had also been reported, with an inner Cr_2O_3-like structure covered by an outer $Cr(OH)_3$ film [9, 30].

As an alternative to in situ deposited films, ex situ electrodepositions of $Cr(OH)_3$ and Cr_2O_3 onto Ti RDE were performed in the present work. The electrodeposition method includes two electrolytes rich in CrO_3. The difference is the use of KNO_3 and H_2SiF_6 for obtaining Cr_2O_3. KNO_3 acts as an oxidizing agent [31] while fluorosilicates stabilizes the oxide phase [32]. It has been reported that NO_3^- and fluoride compounds catalyze the formation of the oxide phase [32]. Differences between Ti and Ti covered with either $Cr(OH)_3$($Cr(OH)_3$@Ti) or Cr_2O_3 (Cr_2O_3@Ti) were first analyzed with an optical microscope (Fig. 1). In Fig. 1a, the pure Ti surface shows a smooth surface with scratches from the polishing, which are seen already with a ×50 magnification. The $Cr(OH)_3$@Ti film is shown in Fig. 1b and presents a light-gray smooth surface. On the other hand, Cr_2O_3@Ti consists of a dark, rough, and brittle layer (Fig. 1c). After drying, the Cr_2O_3 layer cracks and easily detaches from the electrode surface, revealing a black thin film bound to the substrate (Fig. 1d).

The morphology and chemical composition of the $Cr(OH)_3$@Ti and Cr_2O_3@Ti surfaces were further analyzed with SEM and EDX. The $Cr(OH)_3$ film displays a rather rough surface in the micrometer scale (Fig. 2a), while EDX analyses revealed that Cr and O are present in a ratio close to 1:3 as expected, and that the signal of the Ti substrate accounts for 15 at% of the total atomic composition (Table 2). By contrast, the Cr_2O_3 film presents plate-shaped crystals less than

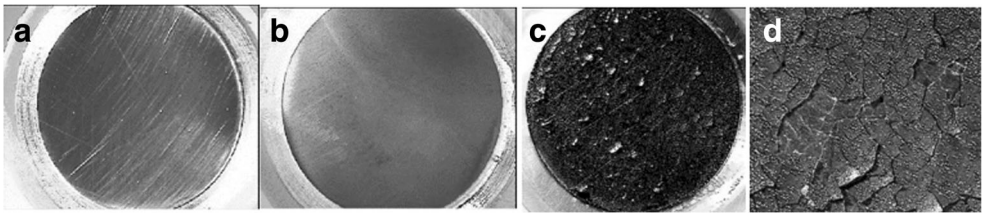

Fig. 1 Titanium electrodes before (**a**) and after $Cr(OH)_3$ (**b**) or Cr_2O_3 (**c**) electrodeposition. **d** Cr_2O_3 after drying at room temperature

1 μm long (Fig. 2b), and EDX measurements show larger amounts of Cr, compared with $Cr(OH)_3$ (Table 2). Still, a smaller amount of Ti, only 2 at%, was recorded during the Cr_2O_3@Ti analyses. EDX is not suitable for obtaining the absolute film thickness due to the interaction volume. However, lower signals from the substrate (under the same acceleration voltage) indicate that the Cr_2O_3 layer is thicker than the $Cr(OH)_3$ layer.

Raman Spectroscopy

Even though EDX analyses have shown the expected Cr/O ratio for both the $Cr(OH)_3$@Ti and Cr_2O_3@Ti phases (Table 2), this is not sufficient to characterize the molecular structure of the films, which we have investigated by Raman spectroscopy. The experiments were carried out by starting with low laser power as suggested in a recent study [33], and the results are summarized in Figs. 3 and 4.

Figure 3 presents a collection of spectra recorded at increasing laser power from an electrode covered with $Cr(OH)_3$. With the lowest laser power (i.e., 0.35 mW), a weak signature is observed at ≈ 850 cm^{-1}, which is characteristic for amorphous $Cr(OH)_3$ [33, 34]. This peak is still visible when a higher laser power is used, although other peaks also appear whose presence is attributed to the in situ formation of Cr_2O_3 as a result of local heating [33]. Compared to the Raman spectra previously recorded for nanoparticles of amorphous $Cr(OH)_3$ (see, e.g., Fig. 6 in [33]), the spectra recorded from $Cr(OH)_3$@Ti appear more noisy (at comparable experimental conditions), which we attribute to the deposited film being very thin. In addition, the spectra recorded at low laser power (e.g., 0.35 and 0.70 mW) display a weak or inexistent peak at 530 cm^{-1} as compared to the intensity at 850 cm^{-1}, a feature that, based on the assignment proposed in [33], suggests films of $Cr(OH)_3$ with partially condensed –OH groups. Moreover, Raman spectra recorded at different spots but using the same laser power (3.50 mW) show some spatial inhomogeneities with a variable proportion of Cr_2O_3 versus $C(OH)_3$ (see Fig. S1 in Supporting Information). We believe that these differences can arise from a variable thickness of the film, and thus different responses to the local heating induced by the laser.

Figure 4 shows the Raman spectra for Ti covered with Cr_2O_3 recorded at the same experimental conditions used in Fig. 3. For increasing laser power, the peaks characteristic of Cr_2O_3 [34–38] gain intensity, as already observed for nanoparticles of Cr_2O_3 [33]. However, differently from the case of nanoparticles [33] the Raman spectrum of Cr_2O_3@Ti recorded with a laser power of 0.7 mW looks featureless, which could be attributed to the film here investigated being amorphous (see x-ray diffractogram in Supporting Information, Fig. S2) and consisting in elongated crystals with a length of ~ 600 nm and a width of less than 100 nm (different from the case of ~ 50-nm-sized nanoparticles grouped together into large particles studied in [33]).

It is known that the electrodeposition of so-called black chromium yields amorphous Cr(III) oxide films/deposits [29, 32, 39], whose actual composition is difficult to determine [32]. XPS has thrown some light towards characterizing this type of films [29, 32, 39, 40], showing either a pure Cr_2O_3 phase [29, 39], a mixture of Cr_2O_3 and $Cr(OH)_3$ [40], or a much more complex matrix of different Cr(III) oxyhydroxides [32]. The XPS investigation made in the present work (Fig. S3) has revealed that the surfaces correspond to

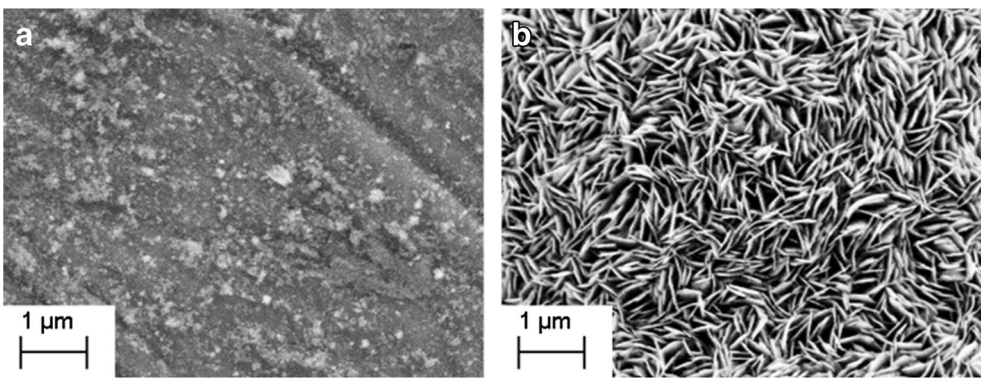

Fig. 2 SEM images of electrodeposited $Cr(OH)_3$ (**a**) and Cr_2O_3 (**b**) onto Ti electrodes at a magnification of 15,000

Table 2 Chemical composition of Ti electrodes covered with electrodeposited $Cr(OH)_3$ and Cr_2O_3

Surface	Cr (at%)	O (at%)	Ti (at%)
Cr_2O_3	37 ± 5	47 ± 10	2 ± 1
$Cr(OH)_3$	20 ± 1	55 ± 8	17 ± 7

Cr(III) oxide-like materials, with some percentage of Cr metal. The complexity of the C1s reference peaks, however, hinders a precise peak positioning and a distinction between $Cr(OH)_3$ and Cr_2O_3 was not possible due to the proximity of the corresponding binding energies [41, 42]. Thus, we assume that the temperature increase induced by light absorption, in this case, promotes amorphous-Cr_2O_3 (or a mixture of oxides) to transform into the more thermodynamically stable crystalline-Cr_2O_3.

To confirm that the transition from amorphous to crystalline Cr_2O_3 was caused by light adsorption at laser intensities higher than 0.7 mW, experiments using 0.7 mW of laser power were carried out at scan times of 50 s (data not shown).

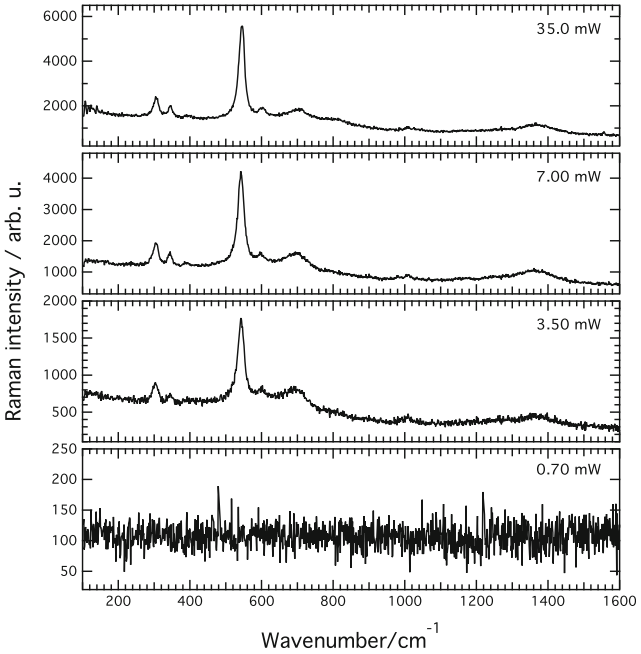

Fig. 4 Raman spectra of electrodeposited Cr_2O_3 onto Ti recorded at four different laser powers

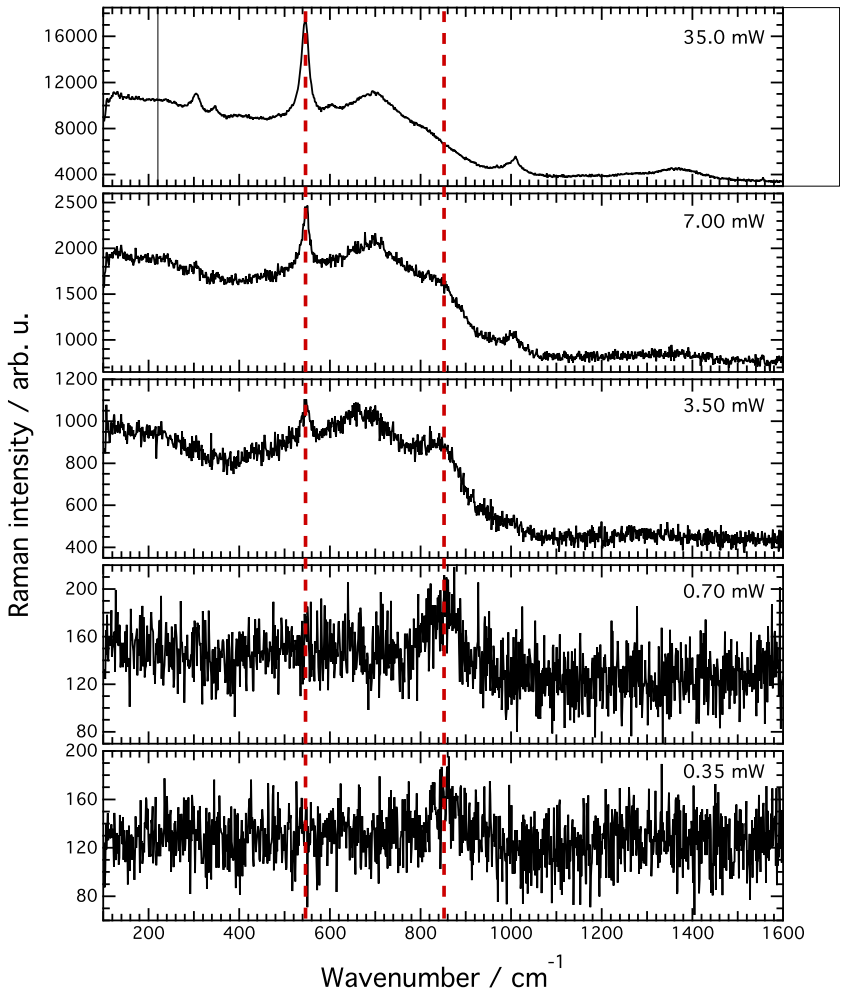

Fig. 3 Raman spectra of $Cr(OH)_3$ electrodeposited onto Ti recorded at a different laser power from the same spot. The line at 855 cm^{-1} marks the characteristic peak for amorphous $Cr(OH)_3$

However, the Raman spectra showed no peaks related to Cr_2O_3, indicating that the temperature increase by Raman laser absorption at 0.7 mW is not enough to crystallize amorphous Cr_2O_3. Also, a pure temperature conversion was studied by electrodepositing Cr_2O_3 onto a Ti disk, which was further inserted in an oven and heated up to 900 °C for 1 h. The results are summarized in Fig. S4 (Supporting Information), and the Raman spectra obtained for the heat-treated sample show the Cr_2O_3 features already with 0.7 mW laser energy.

Electrode Surface Area Estimation

The capacitance of the $Cr(OH)_3$@Ti and Cr_2O_3@Ti electrodes was measured by means of cyclic voltammetry in the non-faradaic region of the voltammogram, between − 0.8 and 0.0 V. Capacitance measurements were used to estimate differences in the active surface area of the electrodes. In Fig. 5, the capacitive currents (I_{Cap}) are plotted as a function of sweep rate (ν). Observe that the currents obtained for Cr_2O_3 (left y-axis) are a thousand times higher than for $Cr(OH)_3$ (right y-axis). The slopes of the curves give the capacitances associated with the $Cr(OH)_3$ (squares) and Cr_2O_3 (diamonds) surfaces. Note that the capacitive currents for the oxide are three orders of magnitude higher than for hydroxide; see also the inset in Fig. 5. The Cr_2O_3 layer displays a capacitance of 1.84×10^{-3} F, while the capacitance of $Cr(OH)_3$ is 3.83×10^{-6} F. It will be seen later that the reduction currents found using Cr_2O_3@Ti electrodes are larger than for $Cr(OH)_3$@Ti electrodes, and that the surface area effect cannot be ignored in further discussions.

Potential sweeps

Potential sweeps performed between 0.0 and − 2.2 V (vs Ag/AgCl) at 50 mV s^{-1} were used to evaluate any possible changes of the $Cr(OH)_3$ and Cr_2O_3 films. Water reduction was the only reaction observed in this potential window, with no further reduction of the Cr(III) or re-oxidation back to chromium(VI) (see Supporting Information, Fig. S5). Cyclic voltammograms at 5 mV s^{-1} were performed to investigate the kinetics of water reduction. The capacitive response was calculated and subtracted from the original data, to allow for a comparison of the onset potential for water reduction. The capacitive currents were calculated using Eq. 10, where j is the current density, ν the sweep rate, C_d the capacitance, and R_0 the solution resistance. The background was fitted to a straight line and subtracted. The corrected currents for water reduction at Ti, $Cr(OH)_3$@Ti, and Cr_2O_3@Ti are summarized in Fig. 6.

$$j = \nu C_d \left[1 - \exp\left(-\frac{t}{R_0 C_d}\right)\right] \tag{10}$$

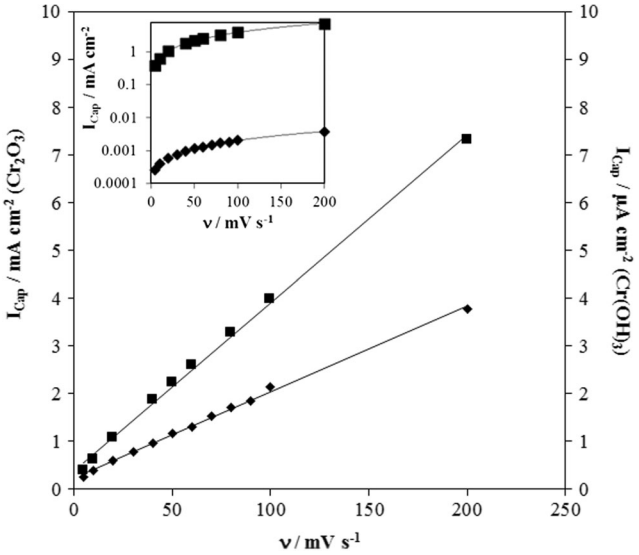

Fig. 5 Capacitive currents as a function of the sweep rate. $Cr(OH)_3$@Ti (squares) and Cr_2O_3@Ti (diamonds). In the inset, the capacitive current is plotted on a logarithmic scale to illustrate the difference in capacitance

From Fig. 6, it is noticeable that the overpotential for water reduction increases in the order Cr_2O_3@Ti < Ti < $Cr(OH)_3$@Ti. At -2 mA, the difference between $Cr(OH)_3$@Ti and Cr_2O_3@Ti is approximately 0.36 V. Ti sits in the middle, indicating that the chromium oxide layer activates the electrode towards water reduction, while the chromium hydroxide deactivates it.

Steady-State Experiments

Tafel slopes and kinetic parameters could not be precisely evaluated based on the potential sweeps, due to the high capacitance. Therefore, potentiostatic measurements were used instead. For these experiments, freshly prepared $Cr(OH)_3$@Ti and Cr_2O_3@Ti electrodes were used. The steady-state current densities (j_{ss}) were measured together with impedance (EIS), at potentials for which water reduction takes place.

The j_{ss} versus potential measurements using Ti, $Cr(OH)_3$@Ti, and Cr_2O_3@Ti are presented in Fig. 7 (symbols). The dotted lines show the data fitting with the kinetic current equation (Eq. 9). It is immediately seen that Fig. 7 reproduces results presented in Fig. 6, i.e., Cr_2O_3 is more active towards water reduction than $Cr(OH)_3$. To ensure a measurable difference between $Cr(OH)_3$ and Cr_2O_3, the experiments were repeated several times (Table 3). By using Eq. 11, the Tafel slopes, charge transfer coefficients (α), and rate constant (k) were calculated and summarized in Table 3, where the number of measurements for each electrode and the uncertainty of the data are also shown.

$$I = -nFAke^{\left(-\frac{\alpha nF}{RT}\eta\right)} \tag{11}$$

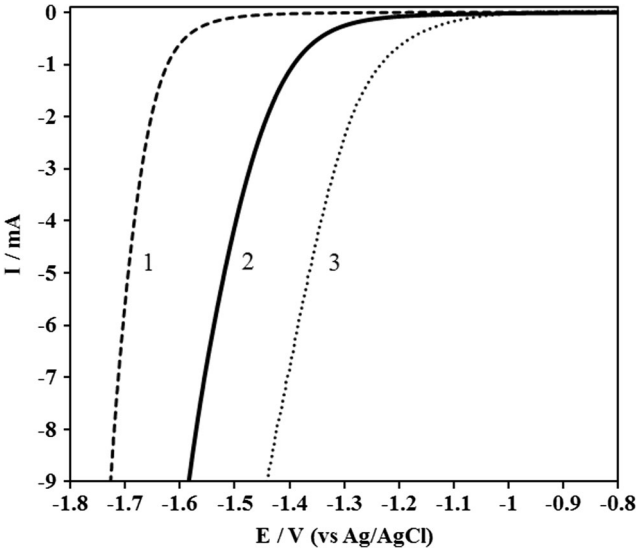

Fig. 6 Water reduction on $Cr(OH)_3$@Ti (1), Ti (2), and Cr_2O_3@Ti (3) electrodes. Sweep rate 5 mV s^{-1}, pH 11, and 0.2 M Na_2SO_4 supporting electrolyte. Electrode rotation rate 3000 rpm

Electrochemical Impedance Spectroscopy

Complex plane plots from 100 kHz to 10 mHz were obtained for every applied potential during the j_{ss} measurements. Complex plane plots obtained for $Cr(OH)_3$@Ti and Cr_2O_3@Ti at each potential are summarized in Fig. 8a, b, respectively. The impedances observed at the highest frequencies were attributed to phase shifts in the instrument and will not be further discussed. The equivalent circuit used to fit the data is given in Fig. 8c. In Fig. 8c, R_0 is the solution resistance, CPE are constant phase elements, and R_1 and R_{ct} are resistances. For the oxide, a phase shift independent of potential is observed prior to the semi-circle. This phase shift is probably due to the porosity of the material. In both cases, $Cr(OH)_3$ and Cr_2O_3, CPE1 and R_1 denote mass transport within the films. While CPE2 and R_{ct} arise from electron transfer, with R_{ct} being the charge transfer resistance.

The faradaic impedance for a kinetically controlled process with only one adsorbed intermediate can be described as in Eq. 12 [43]. Assuming that the reaction mechanism has no coverage dependence with potential, the last term of the equation can be eliminated and the impedance is directly proportional to the R_{ct}.

$$\frac{1}{Z_F} = \frac{1}{R_{ct}} + \frac{\partial I}{\partial \theta}\frac{\Delta \theta}{\Delta E} \tag{12}$$

By plotting log $1/R_{ct}$ versus E, as presented in Fig. 9, a Tafel-like curve is obtained. Linear fits revealed slopes of 266 and 170 mV dec^{-1} for Cr_2O_3 and $Cr(OH)_3$, respectively. These results are in agreement with Tafel slopes found using the steady-state current measurements in Table 3.

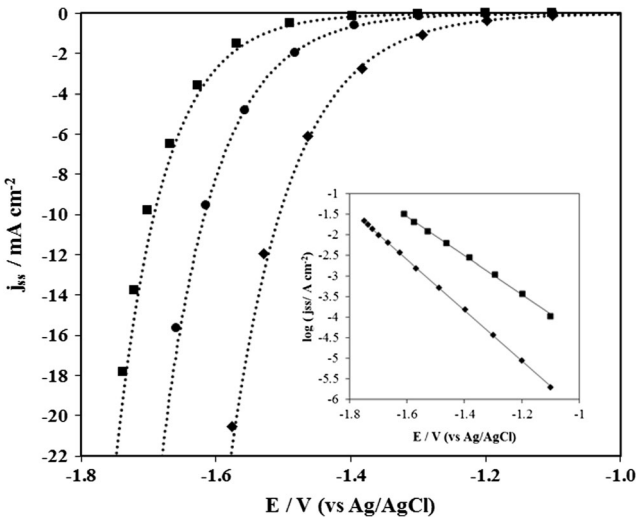

Fig. 7 Steady-state current measurements (symbols) and simulated irreversible one-electron transfer (dotted line). Inset shows the Tafel plots for the j_{ss} experiments. Bare Ti (dots), $Cr(OH)_3$@Ti (squares), and Cr_2O_3@Ti (diamonds)

Reaction Order

The electrochemical reaction orders with respect to OH^- ions were investigated. The plot presented in Fig. 10 was constructed by varying the pH from 9.5 to 12.5, by NaOH addition, and further acidifying back to 9.5 with H_2SO_4, in 0.5 pH steps. The currents were measured at − 1.5 V (vs Ag/AgCl). $Cr(OH)_3$ presents a clear change in slope, indicating a change in the reaction order from zero to − 0.3. Opposite to that, results found for Cr_2O_3 show no change in the reaction order in the pH region investigated. The result from acidifying the solution did not show any dramatic discrepancies and was omitted.

The HER Mechanism

Tafel Slopes

The rate-determining step (rds) for the HER on $Cr(OH)_3$ and Cr_2O_3 films was determined by the Tafel slopes. The Tafel slopes obtained using Cr_2O_3@Ti and $Cr(OH)_3$@Ti were, respectively, − 239 ± 27 and − 145 ± 28 mV dec^{-1} (Table 3), indicating that the first electron transfer is the rds at both surfaces. The low α values indicate that the transition state is shifted to the right on the reaction coordinate axis, and the structure of the activated complex is closer to H_{ads} than H_2O.

The α value for the $Cr(OH)_3$ film is higher than for the Cr_2O_3 film, ~ 0.4 compared with ~ 0.25. A possible explanation for the difference in the transfer coefficient is that water is integrated as part of the $Cr(OH)_3$ film and the film itself is probably involved in the reduction reaction. In this way, the

Table 3 Kinetic parameters for water reduction on both Cr (III) films electrodeposited

	Number of repetitions	Tafel slope[a] (mV dec^{-1})	Charge transfer coef. (α)[a]	Reaction rate (k)[b] (mol cm^{-2} s^{-1})
Cr_2O_3	5	− 239 (± 27)	0.25 (± 0.03)	2.3 (± 1.5) × 10^{-10}
$Cr(OH)_3$	6	− 145 (± 28)	0.41 (± 0.06)	9.9 (± 12) × 10^{-13}
Ti	1	- 180	0.31	8.0 × 10^{-12}

[a] Experimentally obtained

[b] Simulated values

activated complex has an intermediate state between water and H_{ads}. For the Cr_2O_3 film, on the other hand, the reaction occurs at the outmost layer and surface water or water from the solution is involved in the reaction. Therefore, the activated complex becomes closer in structure to the fully reduced form, H_{ads}.

Acid-Base Properties

The mechanism for the HER on oxides/hydroxides can be discussed based on the acid-base properties of the surface. The acid-base equilibrium for oxides in solution is described by the 2pK model [44] as given in Eq. 13. The surface charge of an oxide in solution is governed by the solution pH, and it can be positive, neutral (zero), or negative. The charge is controlled by either protonation or deprotonation of surface oxygen atoms. For Cr_2O_3 and $Cr(OH)_3$, surface charges are not well defined and different numbers are obtained depending on conditions according to Kosmulski [45]. The value for Cr(hydr)oxides is between 7.9 and 10.3. It is difficult to say that there should be a difference between the oxide and the hydroxide, but commonly hydroxides have higher pzc compared to the oxide. If this is the case, the oxide is negative in the entire pH range studied 9.5–12.5, while the hydroxide may have a change in the surface charge. The reaction order shows no dependence for the oxide and for the hydroxide in the low pH range. Hence, a correlation between different α values observed for the hydroxide and for the oxide cannot be made.

$$\begin{aligned} &\equiv Cr{-}OH_2^+ + H_2O \leftrightarrow \equiv Cr{-}OH + H_3O^+ \quad K_{a1} \\ &\equiv Cr{-}OH + H_2O \leftrightarrow \equiv Cr{-}O^- + H_3O^+ \quad K_{a2} \end{aligned} \tag{13}$$

Hydrogen evolution proceeds as shown in Eqs. 14–16. First, adsorption of a proton accompanied with an electron transfer yields a $^* - OH_2$ group (Eq. 14), and hydrogen evolution occurs either by recombination of $2\ ^* - OH_2$ groups (Eq. 15) or by the transfer of a second electron as in Eq. 16. This mechanism was proposed by Hedenstedt et al. [46, 47] on

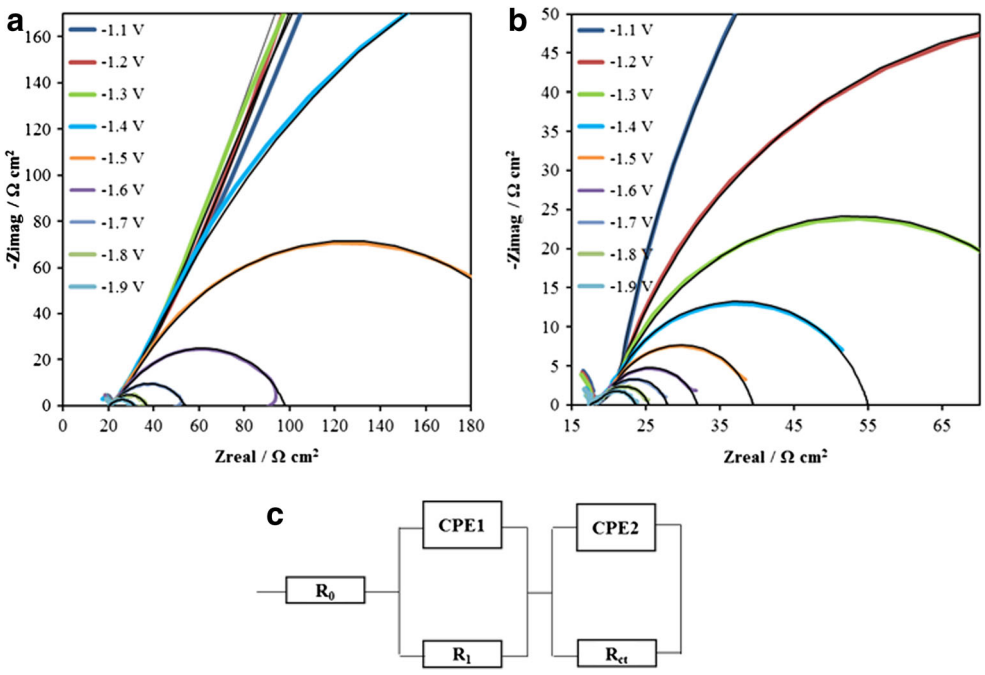

Fig. 8 Complex plane plots of $Cr(OH)_3$@Ti (**a**) and Cr_2O_3@Ti (**b**). Color lines show experimental data fitted (thin black lines) with the equivalent circuit in (**c**)

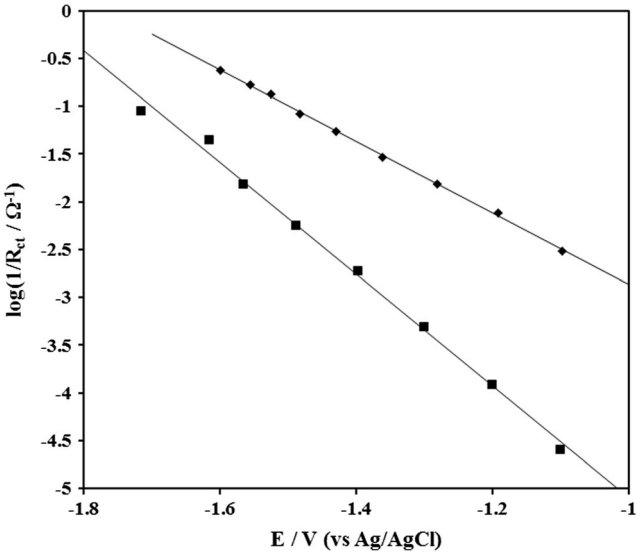

Fig. 9 "Tafel" slopes obtained by EIS measurements. $Cr(OH)_3$@Ti (squares) and Cr_2O_3@Ti (diamonds)

Fe oxides, and used by Larses et al. [48] to investigate the water reduction mechanism on $Fe_{1-x}Cr_xOOH$ and $Cr(OH)_3$ electrodes. In [48], phase diagrams made using density function theory (DFT) demonstrated that M-OH is the most likely structure under HER conditions. Interestingly, they found that the OH coverage increases with increasing Cr content. Taking that into account, a clear distinction between $Cr(OH)_3$ and Cr_2O_3 cannot be made in the acid-base or reaction order point of view. We then assume that the mechanism for HER is the same and follows what is presented in Eqs. 13–16.

$$\equiv Cr{-}OH_2^+ + e^- \leftrightarrow \equiv Cr{-}OH_2 \quad (14)$$

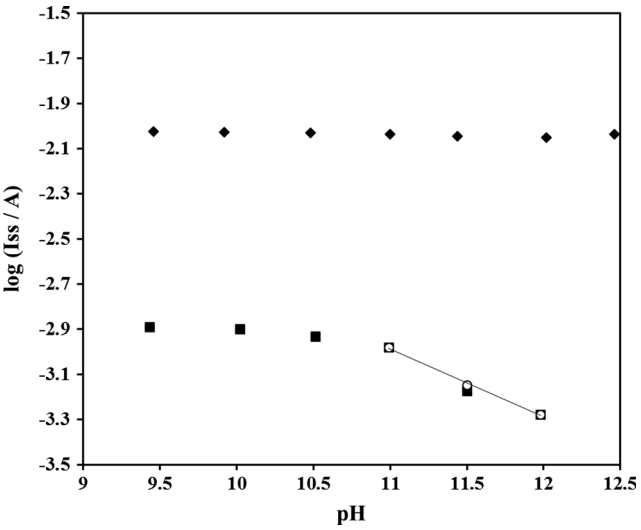

Fig. 10 pH dependence of water reduction currents on $Cr(OH)_3$@Ti and Cr_2O_3@Ti electrodes. $Cr(OH)_3$@Ti (squares) and Cr_2O_3@Ti (diamonds) for titration with hydroxide, and $Cr(OH)_3$@Ti (open dots) for titration with acid

$$2\equiv Cr{-}OH_2 \leftrightarrow \equiv Cr{-}OH + H_2 \quad (15)$$

$$\equiv Cr{-}OH_2 + H_2O + e^- \rightarrow \equiv Cr{-}OH + H_2 + OH^- \quad (16)$$

Reaction Kinetics

The kinetics of the HER were investigated by potential sweeps and steady-state polarization (Figs. 6 and 7). Although the reaction mechanism follows the same path on oxide and hydroxide, the overpotential for the HER is the lowest in the presence of Cr_2O_3, and the highest when Ti is covered with $Cr(OH)_3$. The lower overpotential and low α value observed on Cr_2O_3@Ti can be rationalized to be due to the larger surface area and the lack of water in the Cr_2O_3 crystallites. On the other hand, as water in the $Cr(OH)_3$ structure is involved in the HER, water has to be replaced by water molecules from the solution, otherwise the film will be destroyed. However, this is hampered by the slow ligand exchange of $Cr(OH)_3$ as described by Tang et al. [49] and Rustad and Casey [50]. This is corroborated by the results presented by Larses et al. [48], who showed increased overpotentials for the HER with increasing Cr content in the $Fe_{1-x}Cr_xOOH$ structure.

Conclusion

Hydrogen evolution was investigated on Ti electrodes covered with either $Cr(OH)_3$ or Cr_2O_3. The main outcomes of this work are as follows:

- The composition of the electrodeposited films was revealed by Raman spectroscopy.
- Cr_2O_3 displays lower overpotentials towards water reduction compared to both $Cr(OH)_3$ and bare Ti electrodes.
- For $Cr(OH)_3$, on the other hand, the HER kinetics are slower resulting in the largest overpotentials.
- Structural water is involved in the HER reaction on $Cr(OH)_3$, and the slow kinetics are explained by the slow water exchange rate for Cr(III) complexes.
- On Cr_2O_3, only surface water or water from solution is involved in the reaction, and the low overpotential was rationalized to be due to the high surface area.

This study has shown that in the search for a replacement for Cr(VI) in the chlorate process, both the composition and the morphology of the deposited layer need to be considered to avoid increasing overpotentials for the HER and subsequent environmental issues related to the resulting increase in energy consumption.

Acknowledgements Financial support from the Swedish research council, 621-2010-4035, is gratefully acknowledged.

References

1. H. Vogt, J. Balej, J.E. Bennett, P. Wintzer, S.A. Sheikh, P. Gallone, S. Vasudevan, K. Pelin, Chlorine oxides and chlorine oxygen acids, in *Ullmann's Encyclopedia of Industrial Chemistry* (Wiley-VCH Verlag GmbH & Co. KGaA, 2010)
2. A. Cornell, *Encyclopedia of applied electrochemistry* (Springer-Verlag, New York, 2014)
3. P. Axegård, E. Bergnor, *Environmental performance of modern ECF bleaching* (TAPPI IPBC, Portland, 2011)
4. G. Lindbergh, D. Simonsson, J. Electrochem. Soc. **3094**, 137 (1990)
5. A. Cornell, D. Simonsson, J. Electrochem. Soc. **3123**, 140 (1993)
6. A. Cornell, B. Hakansson, G. Lindbergh, J. Electrochem. Soc. **D6**, 150 (2003)
7. A. Cornell, B. Hakansson, G. Lindbergh, Electrochim. Acta **473**, 48 (2003)
8. G. Lindbergh, D. Simonsson, Electrochim. Acta **1985**, 36 (1991)
9. A. Cornell, G. Lindbergh, D. Simonsson, Electrochim. Acta **1873**, 37 (1992)
10. J. Wullf, A. Cornell, J. Appl. Electrochem. **181**, 37 (2007)
11. K. Hedenstedt, A.S.O. Gomes, M. Busch, E. Ahlberg, Electrocatalysis **326**, 7 (2016)
12. B.V. Tilak, K. Viswanathan, C.G. Rader, J. Electrochem. Soc. **1228**, 128 (1981)
13. J. Landin, *Förfaringssätt vid framställning af klorater och perklorater*, K.P.-o. Registreringsverket, Editor (Sweden, 1892)
14. C. Wagner, J. Electrochem. Soc. **181**, 101 (1954)
15. A.A. Tidblad, G. Lindbergh, Electrochim. Acta **1605**, 36 (1991)
16. N. Krstajić, V. Nakić, M. Spasojević, J. Appl. Electrochem. **77**, 17 (1987)
17. A. Ahlberg Tidblad, J. Mårtensson, Electrochim. Acta **389**, 42 (1997)
18. W.J. Clark, R.L. McCreery, J. Electrochem. Soc. **B379**, 149 (2002)
19. I.M. Kolthoff, A.M. Shams El Din, J. Phys. Chem. **1564**, 60 (1956)
20. J.J. Hatch, A.A. Gewirth, J. Electrochem. Soc. **D497**, 156 (2009)
21. A. Leonárd, R.R. Lauwerys, Mutat. Res. **227**, 76 (1980)
22. R. Saha, R. Nandi, B. Saha, J. Coord. Chem. **1782**, 64 (2011)
23. REACH, No 348/2013 (2013)
24. J. Gustavsson, L. Nylén, A. Cornell, J. Appl. Electrochem. **1529**, 40 (2010)
25. L. Nylén, J. Gustavsson, A. Cornell, J. Electrochem. Soc. **E136**, 155 (2008)
26. J. Gustavsson, G. Lindbergh, A. Cornell, Int. J. Hydrog. Energy **9496**, 37 (2012)
27. M. Li, Z. Twardowski, F. Mok, N. Tam, J. Appl. Electrochem. **499**, 37 (2007)
28. U.C. Lačnjevac, B.M. Jović, L.M. Gajić-Krstajić, J. Kovač, V.D. Jović, N.V. Krstajić, Electrochim. Acta **34**, 96 (2013)
29. M. Aguilar, E. Barrera, M. Palomar-Pardavé, L. Huerta, S. Muhl, J. Non-Cryst. Solids **31**, 329 (2003)
30. H. Tsuchiya, S. Fujimoto, O. Chihara, T. Shibata, Electrochim. Acta **4357**, 47 (2002)
31. E. Barrera, I. Gonzalez, T. Viveros, Sol. Energy Mater. Sol. Cells **69**, 51 (1998)
32. N. Vasudevan, V.K.W. Grips, I. Rajagopalan, Surf. Technol. **119**, 14 (1979)
33. A.S.O. Gomes, N. Yaghini, A. Martinelli, E. Ahlberg, J. Raman Spectrosc. **48**, 1256 (2017)
34. F.D. Hardcastle, I.E. Wachs, J. Mol. Catal. **173**, 46 (1988)
35. P. Li, Z. Zhou, H. Xu, Y. Zhang, Thermochim. Acta **71**, 544 (2012)
36. S. Khamlich, E. Manikandan, B.D. Ngom, J. Sithole, O. Nemraoui, I. Zorkani, R. McCrindle, N. Cingo, M. Maaza, J. Phys. Chem. Solids **714**, 72 (2011)
37. J. Yang, H.F. Cheng, W.N. Martens, R.L. Frost, J. Raman Spectrosc. **1069**, 42 (2011)
38. J. Yang, W.N. Martens, R.L. Frost, J. Raman Spectrosc. **1142**, 42 (2011)
39. M. Aguilar-Sánchez, M. Palomar-Pardavé, M. Romero-Romo, M.T. Ramírez-Silva, E. Barrera, B.R. Scharifker, J. Electroanal. Chem. **128**, 647 (2010)
40. S. Surviliene, A. Cesuniene, V. Jasulaitiene, I. Jureviciute, Appl. Surf. Sci. **837**, 324 (2015)
41. E. Desimoni, C. Malitesta, P.G. Zambonin, J.C. Riviere, Surf. Interface Anal. **173**, 13 (1988)
42. Z.A. Hamid, Surf. Coat. Technol. **3442**, 203 (2009)
43. E. Ahlberg, H. Anderson, Acta Chem. Scand. **1063**, 47 (1993)
44. D.A. Dzombak, F.M.M. Morel, *Surface complexation modeling: hydrous ferric oxide* (Wiley, New York, 1990)
45. M. Kosmulski, Adv. Colloid Interf. Sci. **1**, 238 (2016)
46. K. Hedenstedt, N. Simic, M. Wildlock, E. Ahlberg, J. Electroanal. Chem. **1**, 783 (2016)
47. K. Hedenstedt, J. Bäckström, E. Ahlberg, J. Electrochem. Soc. **H621**, 164 (2017)
48. P. Larses, A.S.O. Gomes, E. Ahlberg, M. Busch, J. Electroanal, Chem. (2017). https://doi.org/10.1016/j.jelechem.2017.09.032
49. Y.Z. Tang, F.M. Michel, L.H. Zhang, R. Harrington, J.B. Parise, R.J. Reeder, Chem. Mater. **3589**, 22 (2010)
50. J.R. Rustad, W.H. Casey, J. Phys. Chem. B **7107**, 110 (2006)